Journal of the Ceramic Society of Japan 130 [8] 627-638 2022
DOI http://doi.org/10.2109/jcersj2.22033

JCS-Japan

SPECIAL ARTICLE-ADVANCEMENTS

The 75th CerSJ Awards for Advancements in Ceramic Science and Technology: Review

Topological analyses of structure of glassy materials toward extraction of order hidden in disordered structure

Yohei Onodera[1,2,†]

[1]Institute for Integrated Radiation and Nuclear Science, Kyoto University, 2–1010 Asashiro-nishi, Kumatori-cho, Sennan-gun, Osaka 590–0494, Japan
[2]Research Center for Advanced Measurement and Characterization, National Institute for Material Science, 1–2–1 Sengen, Tsukuba, Ibaraki 305–0047, Japan

Understanding the structure of disordered materials is still one of the most challenging topics in materials science because of insufficient structural information on experimental data. In this article, recent studies in solving the structure of glassy oxide materials via a combination of quantum beam experiments and computer simulations with the aid of advanced topological analyses are reviewed. To investigate glass structure on the intermediate length scale, three-dimensional atomistic structure models, which reproduce the multiple experimental dataset, were constructed. Furthermore, various topological analyses found that the network topology is an important structural feature for understanding properties of oxide glasses. The comprehensive approach including experimental, computational, and analytical method will be a promising way to probe the hidden order in disordered structure and provide crucial knowledge to design new glass materials with novel characteristics.

Key-words : Oxide glasses, Structure, Neutron diffraction, X-ray diffraction, Topology

[Received February 26, 2022; Accepted May 27, 2022]

1. Introduction

The structure of glassy, liquid, and amorphous materials has no translational periodicity and thus cannot be analyzed based on well-known crystallography. The lack of long-range order in disordered materials makes it difficult to understand the relationship between structure and property. To analyze the structure of disordered materials, measurement of the pair distribution function (PDF) using X-ray diffraction (XRD) and/or neutron diffraction (ND) is the first step. The PDF describes the distribution of distances between atomic pairs and allows us to investigate the structure of disordered materials in real space. A combination of XRD and ND is very powerful in the PDF analysis, because X-rays are sensitive to heavy elements whereas neutrons are indispensable probes for observing light elements.[1)] In the PDF analysis, the scattering intensity is analyzed to give the total structure factor, $S(Q)$, where Q is the magnitude of the scattering vector given by

$$Q = \frac{4\pi \sin\theta}{\lambda}, \tag{1}$$

where 2θ is the scattering angle and λ is the incident wavelength of the X-ray or neutron. The advanced instrumentations at synchrotron and neutron facilities[2)] cover scattering data in a wide Q range, which is achieved by utilizing short-wavelength (high-energy) photons and neutrons, yielding high real-space resolution in the PDF. However, experimentally obtained structural information on disordered materials is limited to pairwise correlations. Hence, it is insufficient to elucidate the intermediate-range order,[3),4)] which exists on a length scale larger than atomic bond lengths (typically beyond 4 Å), in disordered materials even if we used advanced instrumentations at quantum beam facilities.

In recent years, in association with the dramatic advancement of computer performance and modelling techniques, it has been possible to construct reliable three-dimensional (3D) atomistic structure models of disordered materials by a combination of quantum beam experiments and computer simulations.[5)] Moreover, recent progress in the development of atomic configuration analysis tools, especially topological analysis tools focused on rings, cavities, and homologies, has enabled us to extract a structural feature hidden in pairwise correlations from 3D atomistic structure models.[6)] Therefore, it can be said that we have reached a stage where we can systematically discuss the relationship between structure and property in disordered materials via the topological analyses.

In this article, we focus on the structure of glassy oxide materials. In particular, we pick three examples taken from

† Corresponding author: Y. Onodera; E-mail: y-onodera@rri.kyoto-u.ac.jp

our recent literature where structural studies by a combination of quantum beam measurements and computer simulations aided by topological analyses were performed. In these studies, reverse Monte Carlo (RMC)[7] and/or molecular dynamics (MD) simulations were performed to create 3D atomistic structure models that are consistent with the multiple experimental dataset, e.g., diffraction, X-ray absorption, and nuclear magnetic resonance (NMR). These reliable atomistic structure models allowed us to investigate the structure on intermediate-range order in glassy oxide materials via various topological analyses. Moreover, we found that the network topology plays an important role for understanding materials properties in glassy oxide materials. The paper is organized as follows. In section 2, the basic theory for diffraction experiments is briefly described. In section 3, the structure of binary phosphate glass is discussed in terms of the formation of a metallic cation–oxygen network.[8] In section 4, the structure of silica (SiO_2) glass are considered for understanding its diffraction pattern and network topology.[6] In section 5, the behavior of alkali ions in the structure of silicate glasses is discussed to tackle the origin of the mixed alkali effect.[9] Finally, we conclude the paper and consider future prospects for extracting the hidden order in the structure of disordered materials in section 6.

2. Diffraction theory

In XRD and ND measurements on disordered materials containing n chemical species, structural information is contained in the total structure factor,[1),2)]

$$S(Q) = 1 + \frac{1}{|\langle W(Q)\rangle|^2}\sum_{\alpha=1}^{n}\sum_{\beta=1}^{n} c_\alpha c_\beta w_\alpha^*(Q) w_\beta(Q)[S_{\alpha\beta}(Q) - 1], \quad (2)$$

where c_α is the atomic fraction of chemical species α; $w_\alpha(Q)$ is either a Q-dependent atomic form factor with dispersion terms in XRD or a Q-independent coherent scattering length in ND and is, in general, a complex number; $S_{\alpha\beta}(Q)$ is a partial structure factor; and

$$\langle W(Q)\rangle = \sum_\alpha c_\alpha w_\alpha(Q). \quad (3)$$

The corresponding real-space information is contained in the PDF, $g(r)$, which is obtained by a Fourier transform of $S(Q)$,

$$g(r) = 1 + \frac{1}{2\pi^2 r\rho}\int_{Q_{\min}}^{Q_{\max}} Q(S(Q) - 1)\sin(Qr)M(Q)dQ, \quad (4)$$

where r is the distance in real space, ρ is the atomic number density, and $M(Q)$ is the Lorch[10] modification function given by $M(Q) = \sin(\pi Q/Q_{\max})/(\pi Q/Q_{\max})$ for $Q \le Q_{\max}$ and $M(Q) = 0$ for $Q > Q_{\max}$, where $Q_{\max}$ is the maximum value of Q. A similar Fourier transform relation can be established between partial structure factors $S_{\alpha\beta}(Q)$ and partial PDFs $g_{\alpha\beta}(r)$. The structure of a disordered material containing n chemical species is described by $n(n+1)/2$ of these partial PDFs. The total correlation function, $T(r)$, which is widely used to investigate the structure of oxide glasses, is given by

$$T(r) = 4\pi r\rho g(r). \quad (5)$$

An important reason to prefer the use of $T(r)$ which scales as r, as opposed to functions such as $g(r)$ which scales as a constant, is that it is broadened symmetrically by thermal motion in the harmonic approximation.[11] In other words, $T(r)$ is more useful than $g(r)$ for peak fitting.[12] By using a real-space function, it is possible to obtain interatomic distances and coordination numbers.[2),5)] To obtain structural information with sufficient resolution in real space, it is necessary to measure $S(Q)$ up to the higher-Q region since a higher real-space resolution is achieved with a larger $Q_{\max}$.[13]

3. Formation of metallic cation–oxygen network in binary phosphate glass with anomalous thermal expansion coefficients

Oxide glass prepared by melt-quenching is usually composed of network former (NWF) and network modifier (NWM) groups.[14] Phosphorus pentoxide (P_2O_5) is generally classified into the NWF group along with SiO_2, B_2O_3, and GeO_2 from the viewpoint of glass-forming ability. However, P_2O_5 differs from other NWF oxides since the P=O bond allows the delocalized electrons in phosphate glasses.[15)–17)] Phosphate glass frequently has poor chemical durability,[18] but has a significant potential for several practical applications owing to its unique physical and structural properties.[19)–23)] In contrast to the conventional NWF oxides, several metal oxides, which can act as either NWF or NWM depending on the glass composition, are classified into intermediate groups.[14] Zinc oxide is classified as being part of the intermediate group. In the case of zinc phosphate (ZP), monolithic bulk glass can be obtained although the P_2O_5 content is < 33.3 mol %. ZP exhibits low-melting point properties and does not contain any hazardous cations, such as lead and fluorine. Therefore, ZP glass is a promising material for use as lead-free sealing glass[24),25)] or as a good host for emitting centers.[26),27)]

The structure of ZP glass has been extensively studied by various methods. Several groups have performed structural analyses using ND and XRD with the aid of RMC modeling.[28)–30)] Those studies indicated the zinc in ZP glass to be in the four-coordinated state. On the other hand, several previous investigations have shown that a metallic cation has a small coordination number in glass,[31)–35)] since the rigid glass network enables the metastable species of metallic cation to be sustained in the glass matrix. Therefore, the modeling of a reliable atomic arrangement in ZP glass based on metallic cation-specific experimental data and conventional diffraction data is essential for understanding the network structure consistent with the coordination state of the zinc. Onodera et al. constructed reliable atomic configurations of ZP glasses from the viewpoint of 3D network linkage, that is, the connectivity of each oxide by the combination of ^{31}P magic angle spin-

ning (MAS) NMR, Zn K-edge extended X-ray absorption fine structure (EXAFS), XRD and ND data, and RMC simulation. Moreover, they discussed the relationship between several properties and the glass structure.[8)]

For glass networks that are similar, the glass with the lower glass transition temperature, T_g, generally exhibits a higher thermal expansion coefficient.[36),37)] However, the thermal expansion coefficients of ZP glasses increase with increasing ZnO fraction (a higher T_g glass exhibits a higher thermal expansion coefficient).[8)] This anomaly of the thermal expansion coefficient suggests that the glass networks might differ depending on the ZnO fraction. The combination of ^{31}P MAS NMR, Zn K-edge EXAFS, XRD and ND data, and RMC simulation applied to $60ZnO–40P_2O_5$ (60ZP) and $70ZnO–30P_2O_5$ (70ZP) glasses has made it possible to determine their structures and enabled us to find that the thermal expansion coefficient is sensitive to the substitution of the phosphate chain network by a network consisting of Zn–O units in zinc-rich glass.

The RMC simulation was performed using XRD, ND,[28)] and EXAFS data with several chemical coordination states around a phosphorus, utilizing the results of ^{31}P MAS NMR, which can provide the information on the Q^n ratio [where n is the number of bridging oxygen (BO) atoms in a tetrahedral unit, e.g., SiO_4 and PO_4]. **Figure 1** shows the experimental neutron and X-ray total structure factors $S^{N,X}(Q)$ and EXAFS $k^3\chi(k)$, respectively, of 60ZP and 70ZP glasses along with those obtained by the RMC simulation. There is good agreement between the experimentally determined and RMC-modeled data of 60ZP and 70ZP glasses, as shown in Fig. 1. The Q^n ratio, as calculated from the area of each peak in the ^{31}P MAS NMR spectra of 60ZP and 70ZP glasses, shows that the number of Q^2 species decreases significantly as the amount of ZnO increases, indicating that the PO_4 units no longer form a glass network for 70ZP glass. Note that the Q^n distributions, that is, Q^0:Q^1:Q^2:Q^3:Q^4 ratios of 0.8:49.8:49.0:0.4:0 and 33.8:65.8:0.4:0:0, obtained from the RMC models for 60ZP and 70ZP glasses, respectively, concurred with the results of ^{31}P MAS NMR. Oxygen coordination numbers around a zinc atom, $N_{Zn–O}$, of 3.6 and 3.8 were calculated from the RMC models at atomic distances of up to 2.4 Å for the 60ZP and 70ZP glasses, respectively. The Zn–O coordination numbers obtained from the RMC models agree with those determined experimentally by EXAFS, which is very sensitive to the Zn–O coordination, but are smaller than some of the values in previous studies.[28)–30)] Accordingly, it is demonstrated that the RMC models are reliable not only in a short range, e.g., Zn–O coordination, but also in an intermediate range, including the connectivity of PO_4 tetrahedra.

To understand the network connectivity in detail in the RMC models, the connectivity of PO_4 tetrahedra and Zn–O polyhedra was analyzed. **Figures 2**(A) and 2(B) show the 3D linkage of the phosphate network in terms of the chain length, as calculated from the total number of atoms in each phosphate. Figure 2(A) shows the fraction of Q^1 units and Q^2 chains of PO_4 tetrahedra in 60ZP glass and a typical RMC-modeled Q^2 chain [inset of Fig. 2(A)]. On the other hand, as can be seen in Fig. 2(B), 70ZP glass consists of only isolated PO_4 tetrahedra (Q^0) and P_2O_7 dimers (Q^1). Thus, the RMC models reproduce the modification of the 3D phosphate network observed by ^{31}P MAS NMR. The total number of atoms constituting the Zn_xO_y units [Figs. 2(C) and 2(D)] was calculated to elucidate the origin of the glass network in ZP glass with low amounts of NWF. As shown in Figs. 2(C) and 2(D), the Zn_xO_y units do not form a network in the 60ZP glass, and the size of the fragment [consisting of up to 41 atoms, as shown in the inset of Fig. 2(C)] is <20 Å. In contrast, 10 % of the Zn_xO_y units in 70ZP glass form networks consisting of more than 40 atoms, as manifested by their atomic configurations consisting of up to 1300 atoms, as shown in the inset of Fig. 2(D). The unusual network structural units consisting of Zn_xO_y polyhedra can be attributed to the smaller oxygen coordination number around the zinc atom than that in the ZnO crystal. In other words, the high glass-forming ability of 70ZP glass stems from this small oxygen coordination. It is suggested that the small Zn–O coordination number is a signature of the NWF, according to Zachariasen's rule,[14)] in the RMC model for 70ZP glass. The present findings regarding the 3D network formation of Zn_xO_y units indicate that interplay between the PO_4 tetrahedra and Zn–O polyhedra is

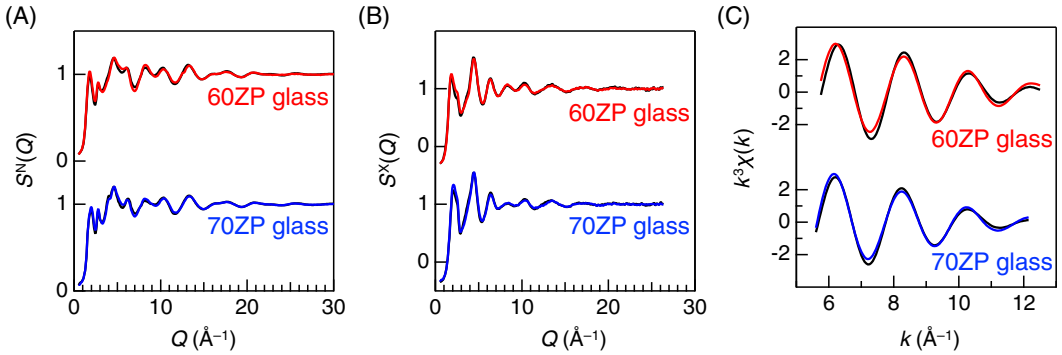

Fig. 1. (A) Neutron total structure factors, $S^N(Q)$, (B) X-ray total structure factors, $S^X(Q)$, and (C) Zn K-edge EXAFS $k^3\chi(k)$ for 60ZP and 70ZP glasses. Reproduced from Ref. 8) (CC BY 4.0). The EXAFS $k^3\chi(k)$ were obtained by back–Fourier transform of the first coordination peak in Fourier-transformed EXAFS data. Black curve, experimental data; colored curve, RMC model.

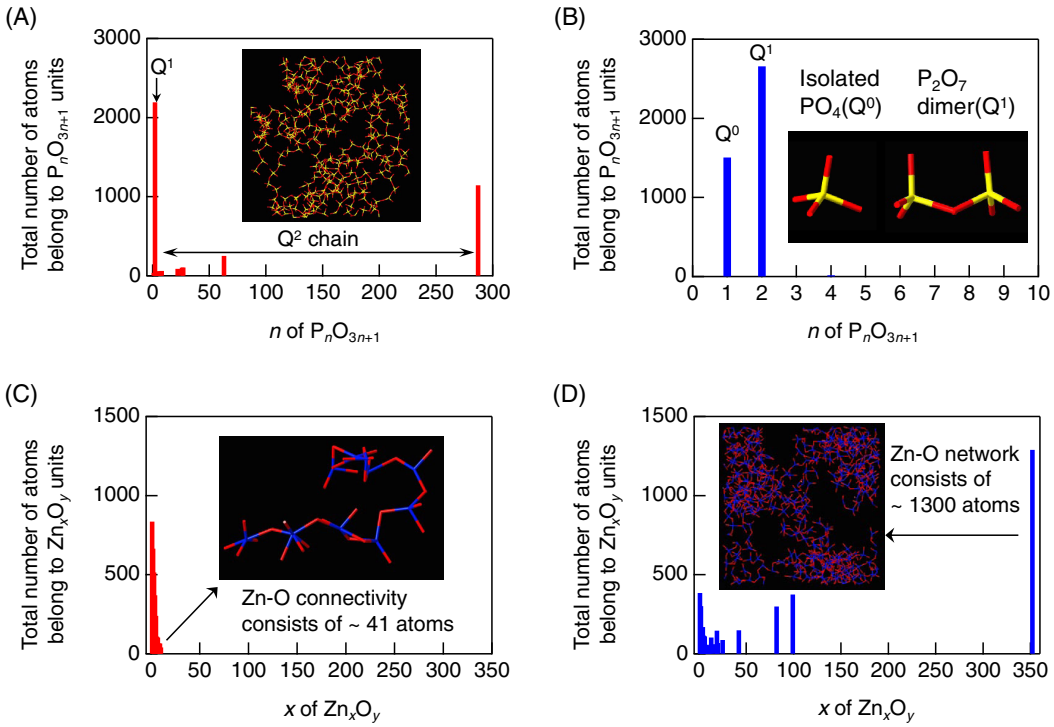

Fig. 2. Size distribution of PO_4 tetrahedral chains in (A) 60ZP glass and (B) 70ZP glass. Size distribution of Zn_xO_y polyhedral chains in (C) 60ZP glass and (D) 70ZP glass. Reproduced from Ref. 8) (CC BY 4.0). Zn, P, and O atoms are shown in blue, yellow, and red, respectively.

important not only for forming glass but also for tuning the physical properties of glass. Such interplays related to the formation of the glass network in oxide glass have been reported for $CaO–Al_2O_3$,[33] $V_2O_5–P_2O_5$[35] glass systems. For instance, in $V_2O_5–P_2O_5$ glass, Aoyagi et al. reported that the glass network formed by the interplay between PO_4 tetrahedra and VO_x polyhedra brings about the improvement of water durability, thermal stability, and hardness.[35] Furthermore, in zinc-rich glass in $ZnO–P_2O_5$ system, it was found that the thermal expansion coefficient sensitively reflects the substitution of the phosphate chain network by a network formed of Zn_xO_y units.

4. Understanding diffraction patterns and uncovering network topology in silica glass

Typical glass-forming materials, e.g., SiO_2, GeO_2, and P_2O_5, have a network structure in which atoms are connected with covalent bonds. For instance, the short-range structure in glassy (*g*-)SiO_2 is a SiO_4 tetrahedron, and the interconnection of SiO_4 tetrahedra forms a network by the sharing of oxygen atoms at the corners. This polyhedral motif is manifested by a first sharp diffraction peak (FSDP) and a principal peak (PP) in structure factor $S(Q)$.[38] It is well known that the FSDP of *g*-SiO_2 is related to the formation of the random network model of Zachariasen[14] and the model was extended to silicate glass by Mei et al.[39] Currently, attempts are being made to understand diffraction patterns from disordered materials measured at synchrotron and neutron facilities, along with the aid of topological analyses based on atomic configurations obtained from RMC and/or MD simulations, which reproduce experimental diffraction data.[6]

The neutron total structure factor, $S^N(Q)$, for *g*-SiO_2[40] is shown in **Fig. 3**(A) together with the X-ray total structure factors, $S^X(Q)$, for amorphous (*a*-)Si[41] and *g*-$Cu_{50}Zr_{50}$.[6] Note that Q is scaled by the nearest-neighbor distance, d, observed in real-space functions to eliminate the effect of atomic size on diffraction pattern. $S^N(Q)$ for *g*-SiO_2 exhibits a three-peak structure: Q_1 (FSDP), Q_2 (PP), and Q_3 [Fig. 3(A) bottom]. $S^X(Q)$ for *a*-Si, possessing a fully tetrahedral network, shows Q_2 and Q_3 [Fig. 3(A) middle], whereas only Q_3 is observed in $S^X(Q)$ for *g*-$Cu_{50}Zr_{50}$ [Fig. 3(A) top], which has a typical dense random packing (DRP) structure.[42–44] As mentioned previously, the network structure of *g*-SiO_2 consists of SiO_4 tetrahedra with shared oxygen atoms at the corners, giving rise to the generation of cavities (empty spaces) owing to the chemical contrast between silicon (fourfold) and oxygen (twofold) atoms. The surface based cavity[45] extracted from the RMC-MD model of *g*-SiO_2 is visualized in Fig. 3(B) together with the cavity size distribution [Fig. 3(C)]. The cavity volume ratio of 33 % and the cavity size distribution indicate that a large cavity is formed in the structure of *g*-SiO_2. These structural features are manifested by the appearance of a FSDP. Therefore, it is shown that the FSDP in *g*-SiO_2 is the signature of the arrangement of tetrahedra with the periodicity given by $2\pi/Q_{FSDP}$, where Q_{FSDP} is the position of the FSDP, as illustrated in **Fig. 4**. It is possible to recognize a periodicity of ~4 Å (indicated by cyan arrows) with a coherence length of ~10 Å (indi-

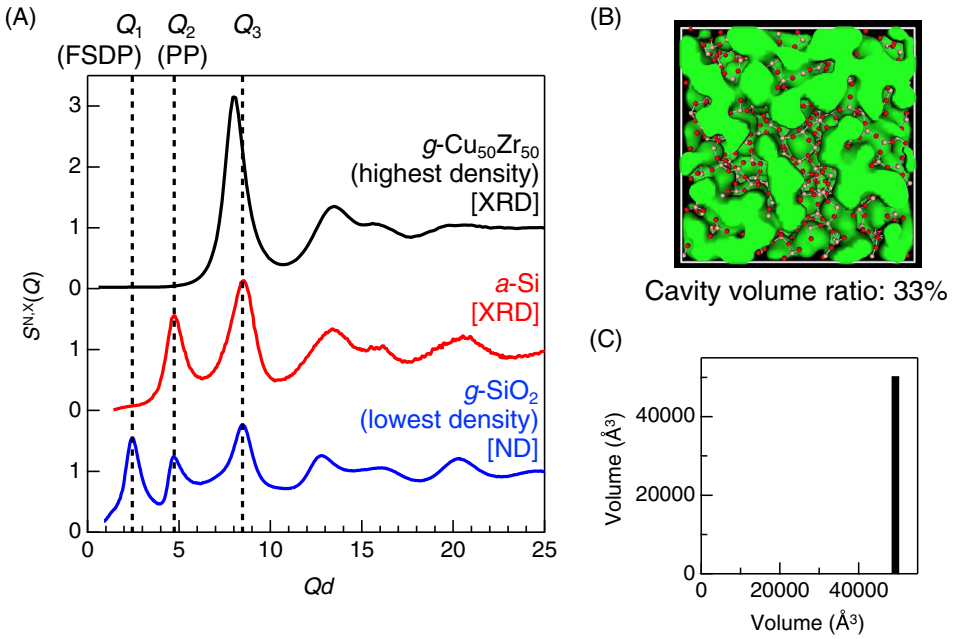

Fig. 3. (A) Neutron and X-ray total structure factors, $S^{N,X}(Q)$, for g-$Cu_{50}Zr_{50}$ (XRD),[6] a-Si (XRD),[41] and g-SiO_2 (ND)[40] scaled by the nearest-neighbor distance, d, obtained in real-space functions. (B) Visualization of cavities and (C) cavity size distribution in g-SiO_2.

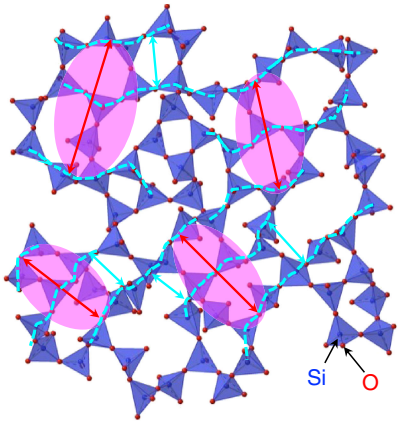

Fig. 4. RMC-MD-generated atomic configuration for g-SiO_2. The thickness of the cell is approximately 9 Å. SiO_4 tetrahedra are shown in blue.

cated by red arrows) given by $2\pi/\Delta Q_{FSDP}$, where ΔQ_{FSDP} is the full width at half-maximum of the FSDP. That is, the FSDP appears as the result of a sparse distribution of planes in polyhedra, because the FSDP of g-SiO_2 diminishes with the increasing pressure associated with densification, that is, the reduction of cavities.[46),47)] The chemical contrast seen in g-SiO_2 is not found in a-Si, whose short-range structural unit is a $SiSi_4$ tetrahedron that results in the absence of the FSDP. The average coordination number in g-$Cu_{50}Zr_{50}$ is approximately 12, which is much larger than those of others, suggesting that the PP is the signature of chemical bonds, because g-$Cu_{50}Zr_{50}$ has no chemical bond in its DRP structure. Recently, Kohara et al. have compared the network topology of liquid and solidified (crystalline and amorphous) Si with those of SiO_2 and concluded that the tetrahedral corner-sharing network of AX_2, in which A is a fourfold cation and X is a twofold anion, as indicated by the FSDP, is an important structural motif for the good amorphous-forming ability and can rule out Si as a good amorphous former.[48)]

To study the network topology of g-SiO_2 in detail, a novel topological analysis, persistent homology,[49)] an emerging mathematical tool for characterizing the shapes of data, was introduced together with the conventional $(Si–O)_n$ ring size distribution analysis.[50),51)] Primitive rings are identified by searching the shortest closed path along with Si–O bonds and cannot be decomposed into smaller rings.[52)] In the calculation of the ring size distribution, the Si–O bond length was set to 1.90 Å. The persistent homology analyses were performed using the Homcloud package.[53)] Given a point cloud in space, persistent homology captures the topological multiscale structures, and those identified are expressed in a persistence diagram (PD). **Figure 5**(A) shows a typical example of the construction of the PD for adjacent regular ring structures. First, each point is replaced with a sphere and the radius is increased from zero to a sufficiently large value. For regular square and hexagonal points whose distance between points is an equal interval, fourfold and sixfold rings appear (birth) simultaneously at radius b_1. Then, fourfold and sixfold rings disappear (death) at radii d_1 and d_2, respectively, and the pair of radii (b, d) for each ring is recorded. The PD is a histogram of the birth–death plane counting of rings at the coordinate (b, d). The one-dimensional PD for a regular square/hexagonal is shown in Fig. 5(B). Further details of the persistent homology are described in Ref. 49). Note that the rings identified in the PD are constructed in a manner different from primitive rings where a closed path

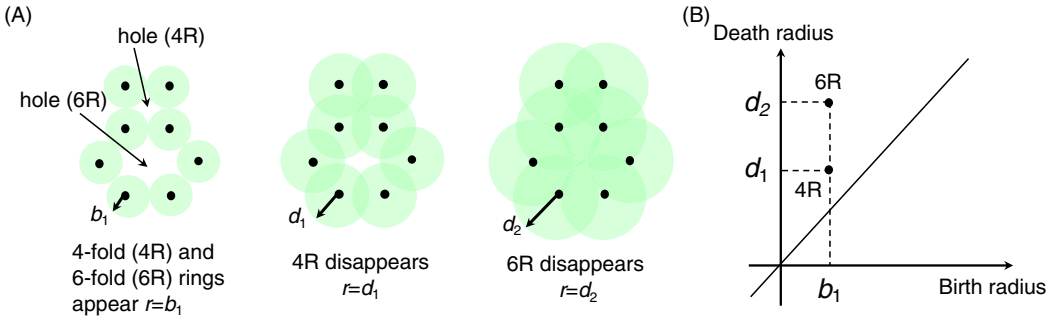

Fig. 5. (A) Appearance and disappearance of a ring for adjacent regular square and hexagonal ring structures. (B) Pairs of birth and death radii for a square and hexagon in the PD.

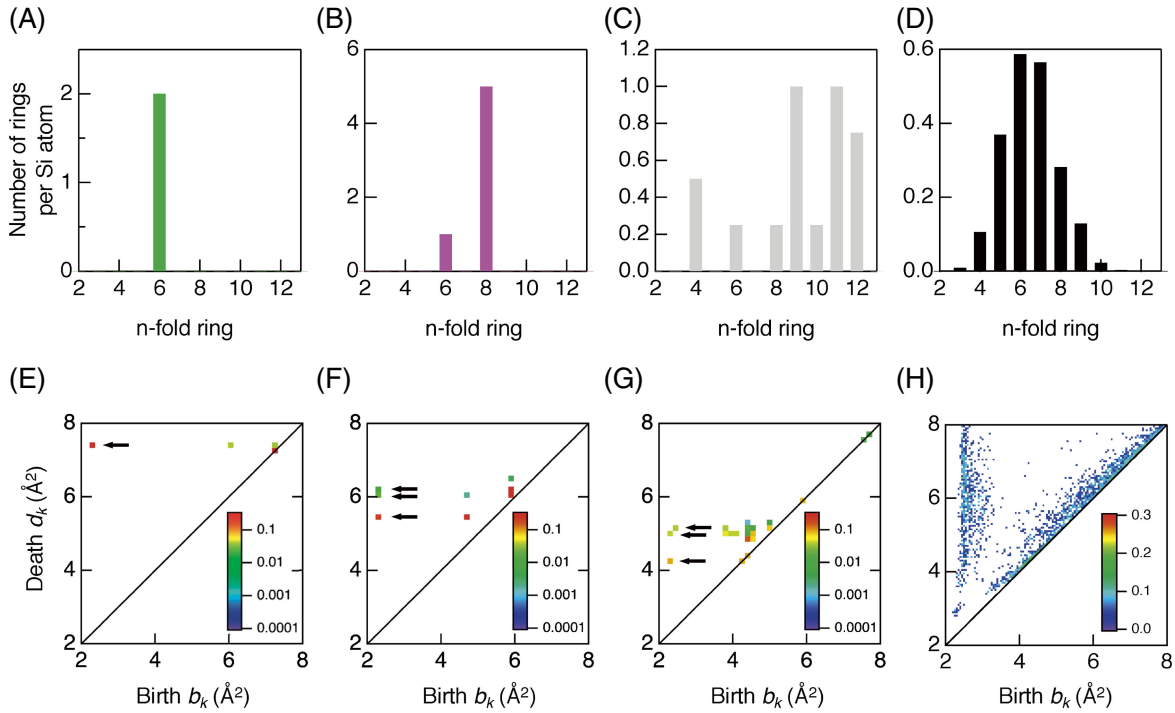

Fig. 6. Primitive ring statistics for (A) α-cristobalite, (B) α-quartz, (C) coesite, and (D) g-SiO_2. Si-centric PDs for (E) α-cristobalite, (F) α-quartz, (G) coesite, and (H) g-SiO_2.

is searched by following the atomic bonds,[52] since the persistent homology identifies rings without searching the atomic bonds. Therefore, in general, rings identified by persistent homology and primitive rings will deliver different information on the atomic arrangement.

Figures 6(A)–6(D) show the primitive $(Si–O)_n$ ring statistics calculated from the crystal structures for α-cristobalite ($d = 2.327\ g\,cm^{-3}$),[54] α-quartz ($d = 2.655\ g\,cm^{-3}$),[55] and coesite ($d = 2.905\ g\,cm^{-3}$),[56] together with that of g-SiO_2 ($d = 2.21\ g\,cm^{-3}$). Note that the structures of all forms of SiO_2 have the network formed of corner-sharing tetrahedral SiO_4 units. α-cristobalite shows only sixfold rings consisting of six SiO_4 tetrahedra [Fig. 6(A)], while α-quartz has a large fraction of eightfold rings in addition to sixfold rings [Fig. 6(B)]. On the other hand, both coesite [Fig. 6(C)] and g-SiO_2 [Fig. 6(D)] exhibit a distribution of different ring sizes, which is a signature of topological disorder according to Gupta and Cooper.[57] The Si-centric PDs of SiO_2 crystals and the glass are shown in Figs. 6(E)–6(H). In SiO_2 crystals and the glass shown here, each structure can be regarded as a silicon network that is decorated by twofold-coordinated oxygen atoms. Therefore, particularly in the persistent homology, the main features in the network topology should be expressed in terms of the point cloud formed of silicon atom coordinates. A systematic change in the Si-centric PDs with density is observed for the crystalline phases in Figs. 6(E)–6(G). In contrast to the crystalline phases, the PD for g-SiO_2 [Fig. 6(H)] has a vertical profile along with the death axis at $b_k \sim 2.2$ Å^2, which is thought to be a signature of a –Si–O–Si–O– network. The comparison between primitive ring size distributions and Si-centric PDs shown in Fig. 6 provides us with comprehensive topological information, because ring statistics analysis is sensitive to the ring size, whereas PDs make it possible to elucidate not only the size but also the shape of rings (how

rings are buckled). The profile observed at birth $b_k = 2.2$ Å^2 in the Si-centric PD for α-cristobalite [Fig. 6(E)] shows a large d_k of 7.4 Å^2, demonstrating that sixfold rings are symmetrical in α-cristobalite. However, the value of d_k decreases with increasing density from α-quartz [Fig. 6(F)] to coesite [Fig. 6(G)], suggesting that the rings are significantly buckled in the high-density crystalline phases. Since all forms of SiO_2 of interest have corner-sharing SiO_4 tetrahedral units, a comparison of α-cristobalite, α-quartz, and coesite with g-SiO_2 in the Si-centric PDs suggests that the glass has not only the homology of a crystalline phase with comparable density (α-cristobalite), but also the homology of higher-density crystalline phases (α-quartz and coesite). Although g-SiO_2 has a distribution of ring sizes [see Fig. 6(D)], Figs. 6(A)–6(C) indicate that crystalline phases exhibit topological disorder with increasing density, because their ring size distributions become broad with increasing density. It is concluded, from the results of a combination of conventional ring statistical analysis and PD analysis, that the vertical profile along with the death axis observed in the Si-centric PD for g-SiO_2 is the result of disorder, because the small death value in the glass implies that SiO_4 tetrahedra are locally more densely packed in the glass than in α-cristobalite, whose density is comparable to that of g-SiO_2. Koyama et al. applied persistent homology analysis to the RMC-MD model for the nonglass-forming liquid, Er_2O_3, and revealed that liquid (l-)Er_2O_3 is homologically similar to the single crystalline phase and that both phases are very densely packed.[58] The behaviors of PDs for g-SiO_2 and l-Er_2O_3 are very different and thus the difference in PDs between g-SiO_2 and l-Er_2O_3 suggests that having the homology of several crystalline phases manifested by the vertical profile in the Si-centric PD is an indicator of the high glass-forming ability of g-SiO_2.

5. Origin of mixed alkali effect in silicate glasses

Silicate glasses are some of the oldest materials in history and are commonly used in the modern glass industry. It is well known that alkali mixing causes several unusual phenomena in silicate glass, that is, when an alkali ion is gradually replaced by another one, some physical properties, for instance electrical conductivity,[59] vary in an extremely nonlinear manner. Although many studies on this "mixed alkali effect" have been reported, the origin of this effect had been unclear because previous studies did not visualize the alkali ion coordination around the nonbridging oxygen (NBO) atoms, which formed by introducing the alkali ions into the SiO_4 tetrahedral network, in the glass structure as being consistent with the multiple experimental dataset. Recently, Onodera et al. investigated the structures of three kinds of $22.7R_2O$–$77.3SiO_2$ glasses (R = Na, K) using ND and XRD to reveal the influence of alkali ions on the glass structure.[9] As alkali ion components, they selected single Na (Na100 glass), single K (K100 glass), and an equal mixture of Na and K ions (Na50K50 glass). The mixed alkali effect in the electrical properties of the alkali silicate glasses was confirmed by measuring the dielectric constants. Indeed, the dielectric constant exhibited a nonlinear trend as a function of the K_2O amount and showed a minimum value in Na50K50 glass.[9] Onodera et al. performed dedicated data-centric structure modeling, employing combined RMC and classical MD simulations (RMC-MD simulations), in accordance with the ND, XRD, and NMR[60] data. Moreover, they carried out persistent homology analysis together with ring size distribution analysis using the 3D atomistic structure models to elucidate the origin of the mixed alkali effect from the behavior of alkali ions around the NBO atoms in the silicate glasses.

Figures 7(A) and 7(B) show the neutron and X-ray total structure factors, $S^{N,X}(Q)$, for three alkali silicate glasses and SiO_2 glass. The prominent FSDP is observed at $Q \sim 1.5$ Å^{-1} in the $S^{N,X}(Q)$ for SiO_2 glass, whereas the FSDP becomes broader when alkali ions are added. The FSDP also appears in the $S^N(Q)$ for the alkali silicate glasses, but the shape of the peak is very complicated. For instance, an extra peak is observed at $Q \sim 0.8$ Å^{-1} in the case of the K100 glass. On the other hand, the FSDP is not visible in

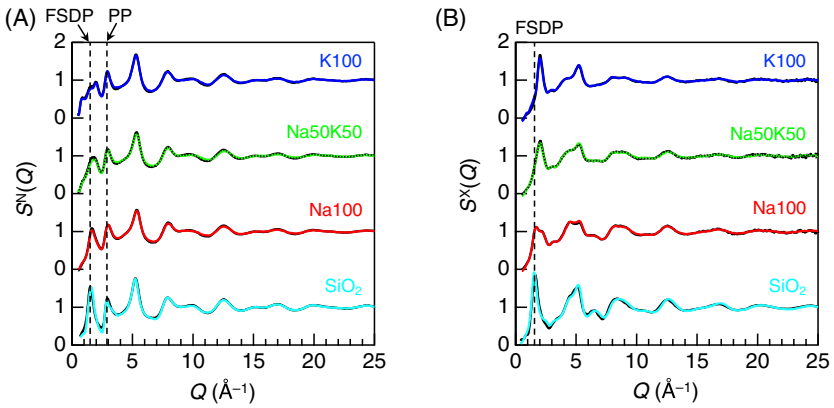

Fig. 7. (A) Neutron total structure factors, $S^N(Q)$, and (B) X-ray total structure factors, $S^X(Q)$, for alkali silicate glasses and SiO_2 glass. Reproduced from Ref. 9) (CC BY 4.0). Black solid curve, experimental data; colored curve, RMC-MD model. Average experimental $S^{N,X}(Q)$ for Na50K50 glass calculated using Na100 glass and K100 glass data are plotted as the dashed black curve.

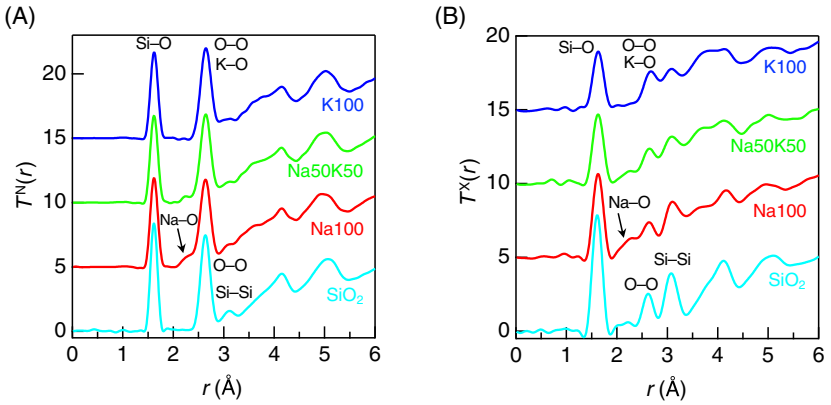

Fig. 8. (A) Neutron total correlation functions, $T^{N}(r)$, and (B) X-ray total correlation functions, $T^{X}(r)$, for alkali silicate glasses and SiO_2 glass. Reproduced from Ref. 9) (CC BY 4.0). The Q_{max} values in a Fourier transformation for neutron and X-ray data are 40 and 25 $Å^{-1}$, respectively.

the $S^{X}(Q)$ for either Na50K50 or K100 glass because of the large weighting factors of potassium for X-rays. It is worth mentioning that the average of the diffraction patterns of Na100 and K100 glasses (black broken curves) is almost identical to the experimental data of both ND and XRD for Na50K50 glass, implying that the mixed alkali effect cannot be easily found in the one-dimensional diffraction data. The neutron and X-ray total correlation functions, $T^{N,X}(r)$, for three alkali silicate glasses and SiO_2 glass are shown in **Figs. 8**(A) and 8(B), respectively. The Si–O correlation peak is located at 1.62 Å with a Si–O coordination number of 4.0 ± 0.1 in all glasses. The Na–O correlation exhibits a small peak at approximately 2.3 Å in the case of Na100 and Na50K50 glasses. The O–O correlation peak and the Si–Si correlation peak are found at 2.63 and 3.08 Å, respectively, in SiO_2 glass, but the peak overlaps the K–O correlation peak for Na50K50 and K100 glasses. It is not easy to extract more detailed information beyond the short-range structure by real-space analysis, demonstrating the limitation of pairwise real-space correlations.

To obtain structural information on the intermediate-range structure beyond the short range, the dedicated data-centric structure modeling with the combination of RMC and classical MD was performed. The starting configurations were created using hard-sphere Monte Carlo (HSMC) simulations with constraints to reproduce the Q^n ratio of the three silicate glasses obtained in the ^{29}Si MAS NMR study.[60] According to the ^{29}Si MAS NMR spectra, the Q^0:Q^1:Q^2:Q^3:Q^4 ratios were 0:0:1.5:55.8:42.7, 0:0:1.2:56.5:42.4, and 0:0:0.8:57.2:42.0 for Na100, Na50K50, and K100 glasses, respectively. After HSMC simulations, RMC simulations were carried out to reproduce the neutron and X-ray $S(Q)$ data with constraints to maintain the Q^n ratio. Following the RMC simulations, the atomic configurations were optimized by the MD simulations with the Morse-type interatomic potential developed by Pedone et al.[61] After MD simulations, all configurations were refined by additional RMC simulations. Further details about RMC-MD simulations are described in our original paper.[9] The final results of the RMC-MD simulations are plotted in Fig. 7 as solid colored curves. A good agreement between the RMC-MD model and experimental data (black solid curves) has been obtained, as shown in Figs. 7(A) and 7(B). It indicates that reliable and accurate structure models for the alkali silicate glasses were constructed by using the combined RMC-MD simulations and reproducing the NMR results and the neutron and X-ray structure factors simultaneously.

To obtain clearer insight to uncover the mixed alkali effect, the persistent homology analysis was applied to the RMC-MD models. First, the alkali-centric PDs for the three alkali silicate glasses were obtained. However, distinguishable differences among the three glasses were not observed in the PDs. On the other hand, the alkali-centric PDs of Na50K50 glass for Na-centric, Na/K-centric, and K-centric data shown in **Figs. 9**(A)–9(C) exhibit a striking difference. Profiles along the diagonal for all the PD data are extracted in Figs. 9(D)–9(F). Both the Na-centric [Fig. 9(D)] and K-centric [Fig. 9(F)] data do not have any characteristic profiles, while only the Na/K centric PD [Fig. 9(E)] has two characteristic profiles at $d_k \sim 5$ and $\sim$10 Å^2. These profiles indicate that Na and K are highly correlated via oxygen in Na50K50 glass, like Na–O–K. Indeed, the connectivity analysis[62] confirmed that 81 % of Na, K, and O atoms form a network in Na50K50 glass. To obtain more crucial structural information associated with the origin of the mixed alkali effect, alkali–oxygen polyhedra with the formation of edge-sharing NBO atoms in alkali silicate glasses are visualized in **Figs. 10**(A)–10(C). A comparison of Na100 [Fig. 10(A)] and K100 [Fig. 10(C)] suggests that the shape of the Na–O polyhedra is planar, whereas that of the K–O polyhedra is polyhedral. According to the calculation of the coordination numbers of the BO and NBO around the alkali ions, the alkali–NBO coordination number is ~2 in both Na100 and K100 glasses, and alkali–BO coordination number is 2.1 in Na100 glass. On the other hand, K100 glass exhibits a larger alkali–BO coordination number, 2.4, and this trend is enhanced in the Na50K50 glass, in which the K–BO coordination number is almost 3. The K–O polyhedra that are highly coordinated with the BO and Na–O polyhedra are highlighted in black in Fig. 10(B), where the potas-

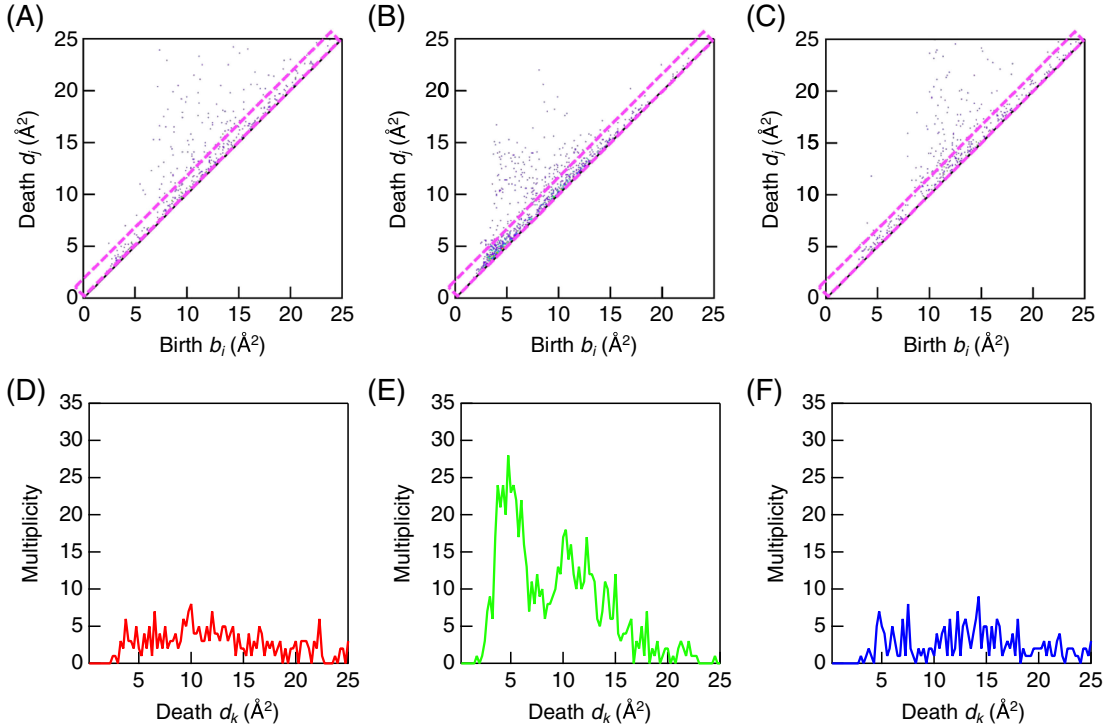

Fig. 9. (A) Na-centric, (B) Na/K-centric, and (C) K-centric PDs for Na50K50 glass. The boxed regions follow the diagonal, and the associated profiles are plotted in (D), (E), and (F), respectively. Reproduced from Ref. 9) (CC BY 4.0).

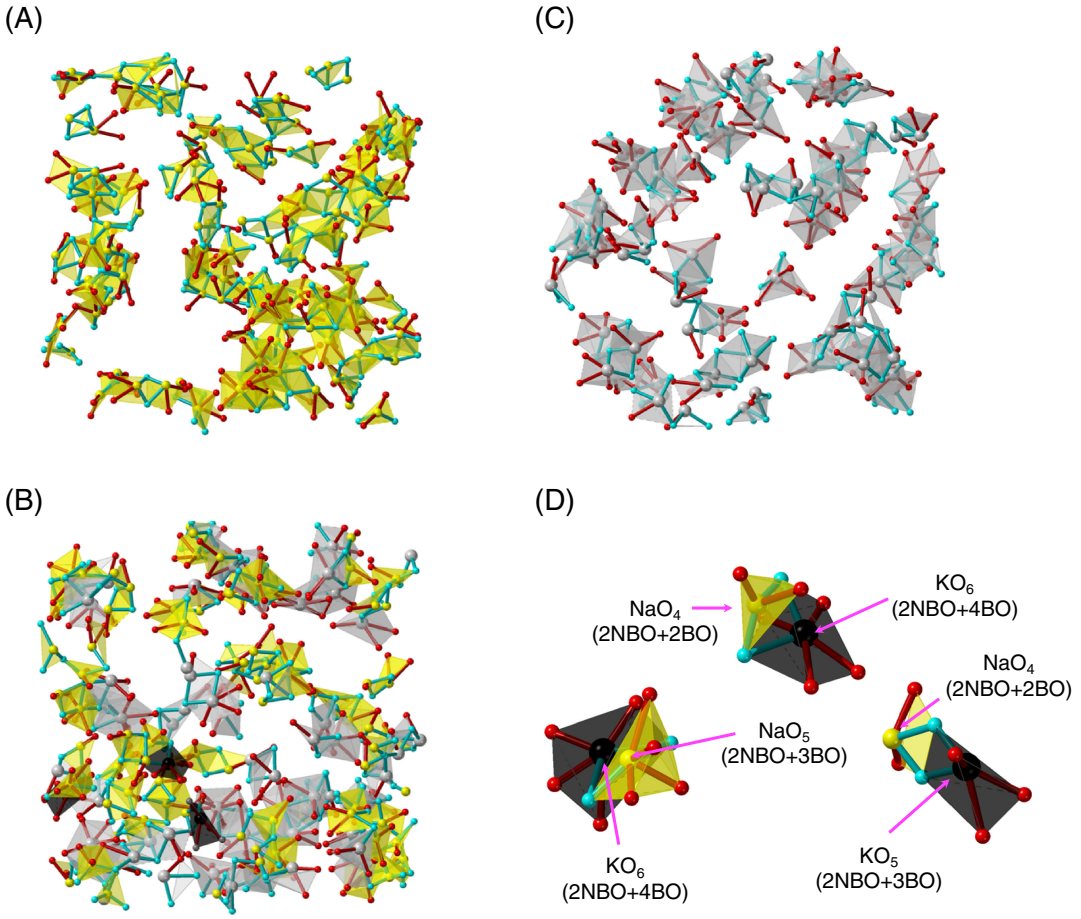

Fig. 10. Visualization of the alkali–oxygen polyhedra around the NBO atoms in (A) Na100, (B) Na50K50, and (C) K100 glasses. (D) Typical bottleneck structures consist of Na–O and K–O polyhedra. Reproduced from Ref. 9) (CC BY 4.0).

sium ion is trapped by a higher number of BO atoms [see Fig. 10(D)]. It is likely that these specific configurations involving NBO atoms are bottlenecks in ionic conduction because the trapped potassium ions disturb the ionic migration. It has been reported that each kind of alkali ion has an independent conduction pathway according to MD simulations on lithium potassium metasilicate glass.[63] Habasaki et al. found that the transfer of alkali ions through different ion sites has a low probability and proposed an interpretation for restricted ion jumping among the sites occupied by other types of ions owing to a mismatch in the occupation energies of unlike alkali ions.[64] The present finding that the local environment of K ions in the highly coordinated K–O polyhedra is significantly different from that of Na ions in the four-coordinated Na–O polyhedra successfully proves their hypothesis. Therefore, Onodera et al. concluded that the local environment of alkali ions associated with alkali connectivity is likely the intrinsic origin of the mixed alkali effect, which supports the modified random network model with the bottleneck structure proposed by Greaves and Sen.[65]

6. Conclusions

In this article, we have reviewed recent studies on the structure of glassy oxide materials revealed by combining quantum beam experiments and structure modeling with topological analyses. By applying advanced topological analyses to reliable atomistic structure models that are consistent with the multiple experimental datasets, network topologies related to the materials properties are discovered. These results highlight the comprehensive approach including experimental, modeling, and analytical techniques enables us to uncover the structural feature hidden in disordered structures beyond the nearest-neighbor correlation length.

Recently, several disordered materials with novel structures and properties have been synthesized by various methods. In 2020, we have reported the unusual behavior of the FSDP in the XRD $S(Q)$ for permanently densified SiO_2 glass synthesized by a hot compression at a pressure of 7.7 GPa and a temperature of 1200 °C.[66] On the other hand, Shang et al.[67] have reported ultrahard bulk amorphous carbon with diamond-like short-/intermediate-range order can be synthesized by heating C_{60} at pressures of 27 GPa and temperatures of 900–1000 °C. Hashimoto et al.[68] very recently have reported the electrochemically prepared Al_2O_3 glass, which can be regarded as a single-component intermediate oxide glass, has a densely oxygen packed structure with a large fraction of edge-sharing polyhedral motifs that is completely outside of Zachariasen's rules. In these studies, quantum beam diffraction, structure modeling, and topological analyses have played significant roles in understanding the relationship between structure and property in novel disordered materials. Therefore, topological analyses combined with quantum beam experiments and structure modeling is an effective approach for questing for fabrication of new glass materials and will promote leading-edge study in glass science.

Acknowledgments The author gratefully acknowledges Dr. Shinji Kohara (National Institute for Materials Science), Dr. Hirokazu Masai (National Institute of Advanced Industrial Science and Technology), Prof. Hiroyuki Inoue (The University of Tokyo), Prof. Atsunobu Masuno (Hirosaki University), Prof. Yasuaki Hiraoka (Kyoto University), Prof. Ippei Obayashi (Okayama University), and many other collaborators for their kind supports and advices.

The work was partially supported by JSPS KAKENHI (Grant Numbers 19K05648), the JSPS Grant-in-Aid for Transformative Research Areas (A) "Hyper-Ordered Structures Science" (Grant Numbers 20H05881), and 'Materials research by Information Integration' Initiative (MI^2I) project of the Support Programme for Starting Up Innovation Hub from Japan Science and Technology Agency (JST).

References

1) H. E. Fischer, H. E. Barnes and P. S. Salmon, *Rep. Prog. Phys.*, 69, 233–299 (2006).
2) S. Kohara and P. S. Salmon, *Adv. Phys.: X*, 1, 640–660 (2016).
3) D. L. Price, S. C. Moss, R. Reijers, M. L. Saboungi and S. Susman, *J. Phys. C Solid State Phys.*, 21, L1069–L1072 (1988).
4) D. L. Price, *Curr. Opin. Solid State Mat. Sci.*, 1, 572–577 (1996).
5) S. Kohara, *J. Ceram. Soc. Jpn.*, 125, 799–807 (2017).
6) Y. Onodera, S. Kohara, S. Tahara, A. Masuno, H. Inoue, M. Shiga, A. Hirata, K. Tsuchiya, Y. Hiraoka, I. Obayashi, K. Ohara, A. Mizuno and O. Sakata, *J. Ceram. Soc. Jpn.*, 127, 853–863 (2019).
7) R. L. McGreevy and L. Pusztai, *Mol. Simulat.*, 1, 359–367 (1988).
8) Y. Onodera, S. Kohara, H. Masai, A. Koreeda, S. Okumura and T. Ohkubo, *Nat. Commun.*, 8, 15449 (2017).
9) Y. Onodera, Y. Takimoto, H. Hijiya, T. Taniguchi, S. Urata, S. Inaba, S. Fujita, I. Obayashi, Y. Hiraoka and S. Kohara, *NPG Asia Mater.*, 11, 75 (2019).
10) E. Lorch, *J. Phys. C Solid State*, 2, 229–237 (1969).
11) A. C. Hannon, W. S. Howells and A. K. Soper, *Inst. Phys. Conf. Ser.*, 107, 193–211 (1990).
12) D. A. Keen, *J. Appl. Crystallogr.*, 34, 172–177 (2001).
13) S. Kohara, K. Ohara, H. Tajiri, C. Song, O. Sakata, T. Usuki, Y. Benino, A. Mizuno, A. Masuno, J. T. Okada, T. Ishikawa and S. Hosokawa, *Z. Phys. Chem.*, 230, 339–368 (2016).
14) W. H. Zachariasen, *J. Am. Chem. Soc.*, 54, 3841–3851 (1932).
15) S. W. Martin, *Eur. J. Sol. State Inor.*, 28, 163–205 (1991).
16) U. Hoppe, *J. Non-Cryst. Solids*, 195, 138–147 (1996).
17) R. K. Brow, *J. Non-Cryst. Solids*, 263–264, 1–28 (2000).
18) B. C. Bunker, G. W. Arnold and J. A. Wilder, *J. Non-Cryst. Solids*, 64, 291–316 (1984).
19) T. Kokubo and J. Takadama, *Biomaterials*, 27, 2907–2915 (2006).
20) P. I. Paulose, G. Jose, V. Thomas, N. V. Unnikrishnan and M. K. R. Warrier, *J. Phys. Chem. Solids*, 64, 841–846 (2003).
21) J. H. Campbell and T. I. Suratwala, *J. Non-Cryst. Solids*,

263–264, 318–341 (2000).
22) Y. C. Yan, A. J. Faber, H. De Waal, P. G. Kik and A. Polman, *Appl. Phys. Lett.*, 71, 2922–2924 (1997).
23) S. Inaba, H. Hosono and S. Ito, *Nat. Mater.*, 14, 312–317 (2015).
24) R. K. Brow and D. R. Tallant, *J. Non-Cryst. Solids*, 222, 396–406 (1997).
25) R. Morena, *J. Non-Cryst. Solids*, 263–264, 382–387 (2000).
26) B. C. Joshi, *J. Non-Cryst. Solids*, 180, 217–220 (1995).
27) H. Masai, Y. Takahashi, T. Fujiwara, S. Matsumoto and T. Yoko, *Appl. Phys. Express*, 3, 082102 (2010).
28) K. Suzuya, K. Itoh, A. Kajinami and C.-K. Loong, *J. Non-Cryst. Solids*, 345–346, 80–87 (2004).
29) U. Hoppe, G. Walter, G. Carl, J. Neuefeind and A. C. Hannon, *J. Non-Cryst. Solids*, 351, 1020–1031 (2005).
30) U. Hoppe, Y. Dimitriev and P. Jóvári, *Z. Naturforsch. A*, 60, 517–526 (2005).
31) S. Kohara, K. Suzuya, K. Takeuchi, C.-K. Loong, M. Grimsditch, J. K. R. Weber, J. A. Tangeman and T. S. Key, *Science*, 303, 1649–1652 (2004).
32) S. Kohara, J. Akola, H. Morita, K. Suzuya, J. K. R. Weber, M. C. Wilding and C. J. Benmore, *Proc. Natl. Acad. Sci. USA*, 108, 14780–14785 (2011).
33) J. Akola, S. Kohara, K. Ohara, A. Fujiwara, Y. Watanabe, A. Masuno, T. Usuki, T. Kubo, A. Nakahira, K. Nitta, T. Uruga, J. K. R. Weber and C. J. Benmore, *Proc. Natl. Acad. Sci. USA*, 110, 10129–10134 (2013).
34) S. Kohara, J. Akola, L. Patrikeev, M. Ropo, K. Ohara, M. Itou, A. Fujiwara, J. Yahiro, J. T. Okada, T. Ishikawa, A. Mizuno, A. Masuno, Y. Watanabe and T. Usuki, *Nat. Commun.*, 5, 5892 (2014).
35) T. Aoyagi, S. Kohara, T. Naito, Y. Onodera, M. Kodama, T. Onodera, D. Takamatsu, S. Tahara, O. Sakata, T. Miyake, K. Suzuya, K. Ohara, T. Usuki, Y. Hayashi and H. Takizawa, *Sci. Rep.*, 10, 7178 (2020).
36) M. Tomozawa, M. Takata, J. Acocella, E. B. Watson and T. Takamori, *J. Non-Cryst. Solids*, 56, 343–348 (1983).
37) J. E. Shelby, *J. Am. Ceram. Soc.*, 66, 225–227 (1983).
38) P. S. Salmon, R. A. Martin, P. E. Mason and G. J. Cuello, *Nature*, 435, 75–78 (2005).
39) Q. Mei, C. J. Benmore, S. Sen, R. Sharma and J. Yargar, *Phys. Rev. B*, 78, 144204 (2008).
40) A. C. Hannon, in "Basic Concepts of Network Glass Structure, Encyclopedia of Glass Science, Technology, History, and Culture", Ed. by P. Richet, R. Conradt, A. Takada and J. Dyon, Wiley Online Library, New York (2021).
41) K. Laaziri, S. Kycia, S. Roorda, M. Chicoine, J. L. Robertson, J. Wang and S. C. Moss, *Phys. Rev. Lett.*, 82, 3460–3463 (1999).
42) J. D. Bernal, *Nature*, 183, 141–147 (1959).
43) J. F. Sadoc, J. Dixmier and A. Guinier, *J. Non-Cryst. Solids*, 12, 46–60 (1973).
44) G. S. Cargill, III and S. Kirkpatrick, *AIP Conf. Proc.*, 31, 339–352 (1976).
45) I. Heimbach, F. Rhiem, F. Beule, D. Knodt, J. Heinen and R. O. Jones, *J. Comput. Chem.*, 38, 389–394 (2017).
46) M. Murakami, S. Kohara, N. Kitamura, J. Akola, H. Inoue, A. Hirata, Y. Hiraoka, Y. Onodera, I. Obayashi, J. Kalikka, N. Hirao, T. Musso, A. S. Foster, Y. Idemoto, O. Sakata and Y. Ohishi, *Phys. Rev. B*, 99, 045153 (2019).
47) A. Zeidler, K. Wezka, R. F. Rowlands, D. A. J. Whittaker, P. S. Salmon, A. Polidori, J. W. E. Drewitt, S. Klotz, H. E. Fischer, M. C. Wilding, C. L. Bull, M. G. Tucker and M. Wilson, *Phys. Rev. Lett.*, 113, 135501 (2014).
48) S. Kohara, M. Shiga, Y. Onodera, H. Masai, A. Hirata, M. Murakami, T. Morishita, K. Kimura and K. Hayashi, *Sci. Rep.*, 11, 22180 (2021).
49) Y. Hiraoka, T. Nakamura, A. Hirata, E. G. Esscolar, K. Matsue and Y. Nishiura, *Proc. Natl. Acad. Sci. USA*, 113, 7035–7040 (2016).
50) S. L. Roux and P. Jund, *Comput. Mater. Sci.*, 49, 70–83 (2010).
51) S. L. Roux and P. Jund, *Comput. Mater. Sci.*, 50, 1217 (2011).
52) C. S. Marians and L. W. Hobbs, *J. Non-Cryst. Solids*, 124, 242–253 (1990).
53) https://homcloud.dev/.
54) J. J. Pluth, J. V. Smith and J. Faber, Jr., *J. Appl. Phys.*, 57, 1045–1049 (1985).
55) K. Kihara, *Eur. J. Mineral.*, 2, 63–77 (1990).
56) L. Levien and C. T. Prewitt, *Am. Mineral.*, 66, 324–333 (1981).
57) P. K. Gupta and A. R. Cooper, *J. Non-Cryst. Solids*, 123, 14–21 (1990).
58) C. Koyama, S. Tahara, S. Kohara, Y. Onodera, D. R. Småbråten, S. M. Selbach, J. Akola, T. Ishikawa, A. Masuno, A. Mizuno, J. T. Okada, Y. Watanabe, Y. Nakata, K. Ohara, H. Tamaru, H. Oda, I. Obayashi, Y. Hiraoka and O. Sakata, *NPG Asia Mater.*, 12, 43 (2020).
59) J. O. Isard, *J. Non-Cryst. Solids*, 1, 235–261 (1969).
60) H. Maekawa, T. Maekawa, K. Kawamura and T. Yokokawa, *J. Non-Cryst. Solids*, 127, 53–64 (1991).
61) A. Pedone, G. Malavasi, M. C. Menziani, A. N. Cormack and U. A. Segre, *J. Phys. Chem. B*, 110, 11780–11795 (2006).
62) S. Kohara, H. Ohno, M. Takata, T. Usuki, H. Morita, K. Suzuya, J. Akola and L. Pusztai, *Phys. Rev. B*, 82, 134209 (2010).
63) J. Habasaki, I. Okada and Y. Hiwatari, *J. Non-Cryst. Solids*, 183, 12–21 (1995).
64) J. Habasaki, I. Okada and Y. Hiwatari, *J. Non-Cryst. Solids*, 208, 181–190 (1996).
65) G. N. Greaves and S. Sen, *Adv. Phys.*, 56, 1–166 (2007).
66) Y. Onodera, S. Kohara, P. S. Salmon, A. Hirata, N. Nishiyama, S. Kitani, A. Zeidler, M. Shiga, A. Masuno, H. Inoue, S. Tahara, A. Polidori, H. E. Fischer, T. Mori, S. Kojima, H. Kawaji, A. I. Kolesnikov, M. B. Stone, M. G. Tucker, M. T. McDonnell, A. C. Hannon, Y. Hiraoka, I. Obayashi, T. Nakamura, J. Akola, Y. Fujii, K. Ohara, Y. Taniguchi and O. Sakata, *NPG Asia Mater.*, 12, 85 (2020).
67) Y. Shang, Z. Liu, J. Dong, M. Yao, Z. Yang, Q. Li, C. Zhai, F. Shen, X. Hou, L. Wang, N. Zhang, W. Zhang, R. Fu, J. Ji, X. Zhang, H. Lin, Y. Fei, B. Sundqvist, W. Wang and B. Liu, *Nature*, 599, 599–604 (2021).
68) H. Hashimoto, Y. Onodera, S. Tahara, S. Kohara, K. Yazawa, H. Segawa, M. Murakami and K. Ohara, *Sci. Rep.*, 12, 516 (2022).

Yohei Onodera is an assistant professor at Institute for Integrated Radiation and Nuclear Science, Kyoto University. He received his M.S. degree in 2006 from Yamagata University and his Ph.D. degree in 2011 from Kyoto University. From 2011 to 2012, he worked as a postdoctoral fellow at Office of Society Academia Collaboration for Innovation, Kyoto University. He worked at Research Reactor Institute, Kyoto University as an assistant professor in 2012–2018. Since 2018, he has been working at Integrated Radiation and Nuclear Science, Kyoto University. His current research interests include the materials science of glass, liquid, and amorphous materials.